

# Microstructural Analysis of Multi-phase Ultra-Thin Oxide Overgrowth on Al–Mg Alloy by High Resolution Transmission Electron Microscopy

Narendra Bandaru<sup>1</sup> · Darshan Ajmera<sup>1</sup> · Krishna Manwani<sup>1</sup> · Sasmita Majhi<sup>1</sup> · Emila Panda<sup>1</sup>

Received: 14 October 2015 / Accepted: 6 June 2016 / Published online: 23 June 2016  
© The Indian Institute of Metals - IIM 2016

**Abstract** High-resolution transmission electron microscopy analyses are carried out to understand the microstructure of the ultra-thin oxide-film grown on a (native) amorphous Al<sub>2</sub>O<sub>3</sub>-coated Al-0.8 at.% Mg alloy substrate at  $T = 600$  K for  $t = 2$  h and at  $pO_2$  of  $1 \times 10^{-2}$  Pa. This oxide-film is found to be non-uniformly thick with thicknesses varying from 1.50 to 4.60 nm. Occasionally, this oxide is found to diffuse into the Al–Mg alloy substrate, forming oxide thicknesses up to 10.5 nm. Overall, this oxide-film is found to consist of a mixed amorphous, (poly) crystalline and an intermediate amorphous-to-crystalline transition regions, with crystalline regions consisting mostly of MgO and the diffused oxide regions into the Al–Mg alloy substrate coated with  $\gamma$ -Al<sub>2</sub>O<sub>3</sub>. These observations are then compared with the experimental results obtained using angle-resolved X-ray Photoelectron Spectroscopy analysis and thermodynamic predictions for the growth of an ultra-thin oxide-film due to dry, thermal oxidation of Al–Mg alloy substrates.

## Keywords

High-resolution transmission electron microscopy (HR-TEM) · Oxidation · Al<sub>2</sub>O<sub>3</sub> · MgO · Ultra-thin

## 1 Introduction

Microstructure of an ultra-thin (<15 nm) oxide film determines its functionality for various applications, like, tunnel junctions, gas sensors, model catalysts and (thin) diffusion barriers [1–9], hence an understanding of this microstructure with respect to the growth conditions is crucial. To this end, extensive investigations have been carried out in the literature [10–32]. However, most of these literature have focused discreetly on the overall microstructure of the oxide-film grown at relatively higher oxidation temperature (>600 K) and at atmospheric conditions on a natively grown oxide (due to aging for a few days at room temperature under atmospheric pressure) without presenting an in-depth analysis on the developed oxide microstructure [18–32]. Others are limited to the thin oxide films grown at lower oxidation temperature of  $T < 600$  K on *in vacuo* sputter cleaned (using inert Ar<sup>+</sup> ion beam to remove the surface contaminants and native oxide present on to the surface) pure metal/alloy substrate [10–17]. Establishing interrelationship between the microstructure of the thin oxide film due to thermal oxidation of a native oxide coated pure metal/alloy substrate with respect to the growth conditions is extremely important as this will help understanding the role of a natively formed barrier oxide layer on the final microstructure of the oxide-film grown due to dry, thermal oxidation.

In an independent study, cleaned (by means of Ar<sup>+</sup> ion sputtering) Al–Mg alloy substrates were oxidized by varying a range of experimental parameters (like, oxidation pressure, temperature, time and alloy composition) in a controlled environment in an ultra-high vacuum (UHV) chamber [15, 33]. Overall, these oxide-films were found to be extremely thin (<3 nm). The oxide-films grown at lower oxide-film thicknesses of  $\leq 0.7$  nm were found to consist of

Narendra Bandaru and Darshan Ajmera have contributed equally to this work.

✉ Emila Panda  
emila@iitgn.ac.in

<sup>1</sup> Department of Materials Science and Engineering, Indian Institute of Technology, Gandhinagar, Ahmedabad 382424, India

only  $\text{Al}_2\text{O}_3$ , whereas, films grown at higher oxide-film thicknesses of  $\geq 0.9$  nm were found to consist of both the  $\text{Al}_2\text{O}_3$  and  $\text{MgO}$ . Additionally, chemical analysis on the natively grown oxide (due to aging at room temperature and under atmospheric pressure for a week) by angle resolved X-ray Photoelectron Spectroscopy (AR-XPS) showed the presence of  $\sim 2.5$  nm thick amorphous  $\text{Al}_2\text{O}_3$  [15]. Thus, in this study, oxide-film was grown by oxidizing the native  $\sim 2.5$  nm thick amorphous  $\text{Al}_2\text{O}_3$ -coated Al-0.8 at.% Mg alloy substrate for  $t = 2$  h in UHV at an elevated temperature ( $T$ ). A reasonably higher  $T$  of 600 K and higher oxygen partial pressure ( $p\text{O}_2$ ) of  $1 \times 10^{-2}$  Pa were used here to understand the nature of the oxide-film growth. Then a detailed high-resolution transmission electron microscopy (HR-TEM) investigation was carried out to understand the developed microstructure, such as, film uniformity, its thickness, chemical constituents, crystallographic orientation relationship with that of the substrate, etc.

This investigation has scientific relevance, as at this higher  $T$ , diffusion controlled rate of anionic and/or cationic species to the reacting interface can be enhanced, thereby increasing the rate of the overall oxidation reaction and forming thicker oxide-film. Further, for the case of the oxidation of the Al–Mg alloy system, where both the alloying constituents have stronger affinity for oxygen (unlike those of the Au–Cu or Pt–Al systems, cases where one element is nobler than the other), it is difficult to predict the type of oxide overgrowth, which may further complicate the overall oxide-film microstructure. Finally, interpreting the influence of the already present barrier *am*- $\text{Al}_2\text{O}_3$  layer on the final microstructure of the oxide-film can be tricky, as at this higher growth  $T$ , competitive thermodynamic and kinetic mechanisms can interplay towards the formation of the entire microstructure. Further, it is unknown whether, the initially present native *am*- $\text{Al}_2\text{O}_3$  crystallizes at these higher  $T$  by subsequent addition of the newly formed  $\text{Al}_2\text{O}_3$  due to reaction between  $\text{Al}^{3+}$  cations and  $\text{O}^{2-}$  anions (thus increasing the overall  $\text{Al}_2\text{O}_3$  thickness) or gets trapped in its original amorphous form along with the newly formed mixed (Al, Mg)-oxide due to oxidation of both the  $\text{Al}^{3+}$  and  $\text{Mg}^{2+}$  cationic species with  $\text{O}^{2-}$  anions.

## 2 Experimental

Single-phase, polycrystalline (average grain size varying in the range of 50–100  $\mu\text{m}$ ), homogeneous Al-0.8 at.% Mg alloy of purity above 99.98 wt% was prepared by successive melting, casting and annealing procedures [33]. Then a disc-shaped specimen (of 10 mm diameter; 1 mm thickness; single-side polished down to 0.05  $\mu\text{m}$ ) was

introduced into a combined UHV system for specimen processing and in situ analysis (base pressure  $< 3 \times 10^{-8}$  Pa). Here, this customized UHV system was equipped with an oxidation chamber, which was interconnected with the AR-XPS analysis chamber and Molecular Beam Epitaxy (MBE) side chamber. The as received specimen was then examined by AR-XPS to identify the chemical constituents present within few nm depth from the sample surface and as a next step, ultra-thin oxide film (thickness  $< 15$  nm; as determined independently by using in situ AR-XPS and ex situ HR-TEM techniques) was grown by exposing this alloy surface for 2 h to pure oxygen gas (of purity  $\geq 99.99990$  vol.%) at a partial oxygen pressure ( $p\text{O}_2$ ) of  $1 \times 10^{-2}$  Pa and at growth temperature  $T = 600$  K in the oxidation chamber [33]. Uniform sample heating was performed using a focused, halogen light beam at the backside of the sample surface, whereas, the sample surface temperature was monitored by use of a type-K thermometer wire that was mechanically pressed on to its surface.

After oxide growth, the oxide-film was subsequently cooled to room temperature and then subjected to in situ AR-XPS analysis in a Thermo VG Thetaprobe system employing monochromatic Al  $K\alpha$  radiation in order to determine the chemical constitution of these oxidic species within this thin oxide-film by varying ( $\alpha$ ,  $\phi$ ) from (23°, 43°) to (83°, 94°) in six ranges of 10° each. Here, ( $\alpha$ ,  $\phi$ ) has been defined as the angles between the directions of the detected photoelectrons and the sample surface normal and the directions of the detected photoelectrons and the incident photon beam, respectively [35]. Next, the grown oxide film was capped by a  $\sim 150$  nm thick Al layer in the UHV MBE side-chamber for ex situ HR-TEM investigation. Next, the oxidized specimen with Al capping layer was removed from the UHV system and, subsequently, a TEM-lamella of 3  $\mu\text{m} \times 4 \mu\text{m}$  size and thickness of about 80–100 nm was cut from the specimen using a dual Focused Ion Beam (FIB Nova Nanolab 600 from FEI company).

Then HR-TEM analysis was carried out on selected grains of the substrate/oxide-film/Al-seal TEM cross-section using a JEOL JEM-ARM 1250 electron microscope with an acceleration voltage of 1250 kV. This lamella was cooled by liquid nitrogen during the entire HR-TEM analysis to reduce any possible microstructural changes in the irradiated area of the specimen due to the high-energy electron beam. Then the negatives of the recorded micrographs were digitized and subsequently length scale of each investigated micrograph was internally calibrated using the known lattice parameter of the bulk Al-0.8 % Mg alloy of 0.40537 nm, as determined by XRD [15]. Finally these micrographs were quantified using Digital Micrograph software.

### 3 Results and Discussion

Figures 1, 2, 3 represent the cross-sectional HR-TEM images of the oxide-film grown on Al-0.8 at.% Mg alloy substrate (i.e., substrate/oxide-film/Al-seal TEM cross-section) at  $T = 600$  K for  $t = 2$  h and at  $pO_2$  of  $1 \times 10^{-2}$  Pa on a natively grown *am*-Al<sub>2</sub>O<sub>3</sub> (of thickness  $2.49 \pm 0.18$  nm; as observed by both the HR-TEM and AR-XPS analyses [15, 33]). This native *am*-Al<sub>2</sub>O<sub>3</sub> has been formed by aging this specimen for 1 week at room

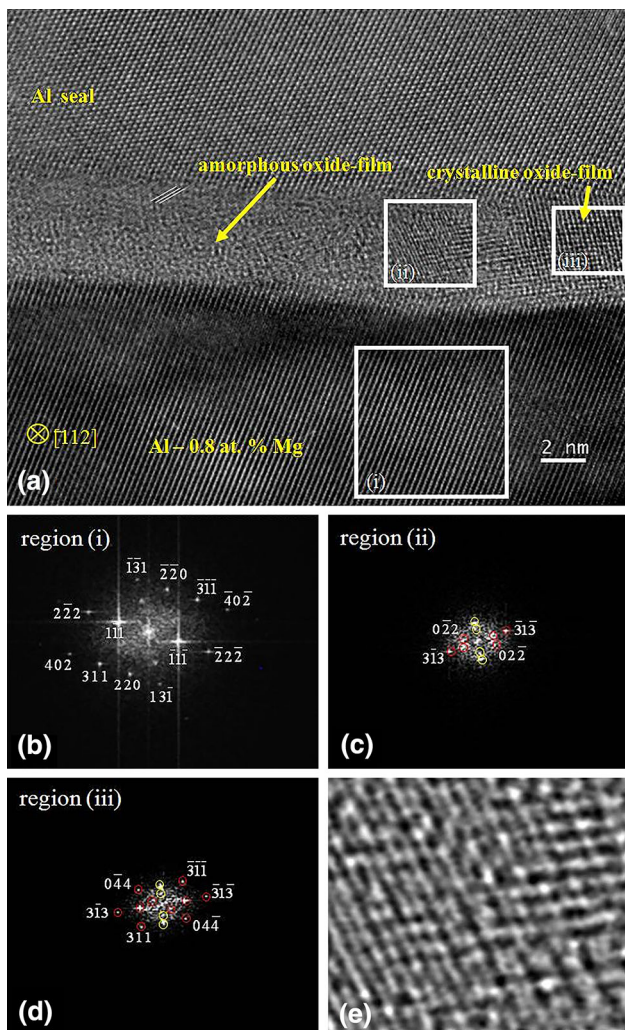


**Fig. 1** (Color Online) **a** HR-TEM micrograph of the oxide film formed by oxidizing the native  $\sim 2.5$  nm thick amorphous Al<sub>2</sub>O<sub>3</sub>-coated Al-0.8 at.% Mg alloy substrate (not shown here) for  $t = 2$  h at  $T = 600$  K and  $pO_2 = 1 \times 10^{-2}$  Pa. The direction of the primary electron beam was along the zone axis  $[\bar{1}12]$  of the investigated grain of the polycrystalline alloy substrate. **b**, **c** and **d** Fourier transformations of the areas (i) (comprising only substrate) and (ii, iii) (comprising only oxide) as indicated in **a**, respectively. **e** Inverse Fourier transformation from the filtered Fourier image of **c** (pertaining to area (iii) in **a**), as obtained after application of a mask, which removes the primary beam and thus selects the ordered regions of the oxide film

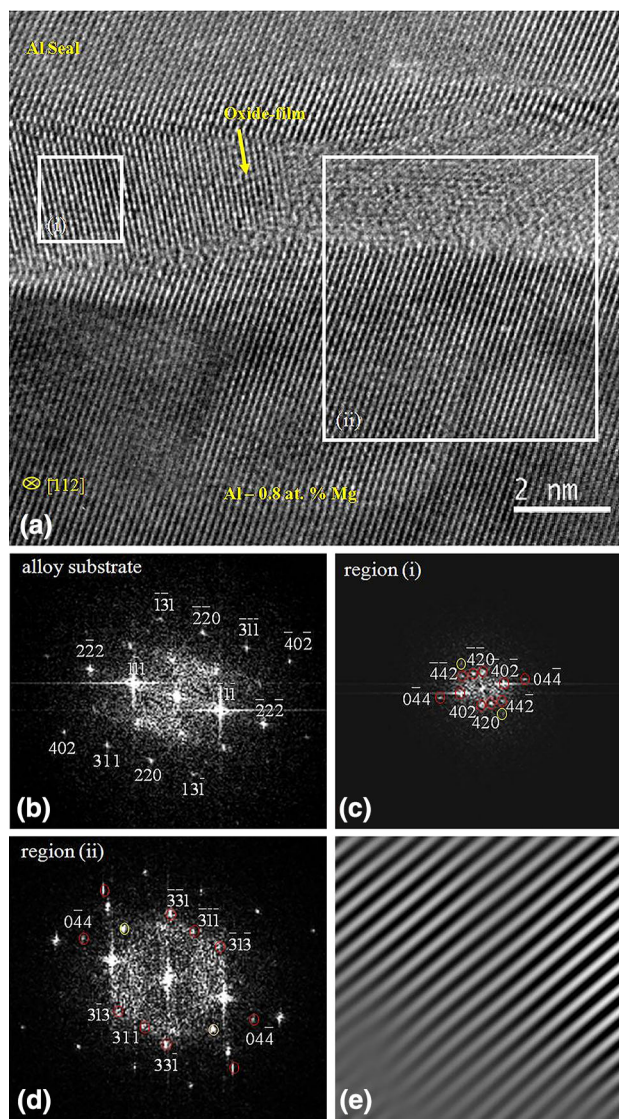


**Fig. 2** (Color Online) **a** HR-TEM micrograph of the oxide film formed by oxidizing the native  $\sim 2.5$  nm thick amorphous Al<sub>2</sub>O<sub>3</sub>-coated Al-0.8 at.% Mg alloy substrate for  $t = 2$  h at  $T = 600$  K and  $pO_2 = 1 \times 10^{-2}$  Pa. The direction of the primary electron beam was along the zone axis  $[\bar{1}12]$  of the investigated grain of the polycrystalline alloy substrate. **b**, **c** and **d** Fourier transformations of the areas comprising only substrate, (i) (comprising only oxide) and (ii) (comprising both substrate and oxide) as indicated in **a**, respectively. **e** Inverse Fourier transformation from the filtered Fourier image of the extra reflections circled by yellow (**d**) (pertaining to area (ii) in **a**), as obtained after application of a mask, which removes the primary beam and the reflections from substrate and the identified oxide and thus selects the unidentified ordered regions of the oxide film

temperature under atmospheric pressure. The thickness of this non-uniformly grown oxide-film is found to vary in the range of (1.50–4.60) nm. Occasionally, at places, the oxide-film is found to have grown and/or diffused into the Al–Mg alloy substrate (see the white dotted marked regions in Fig. 3a) forming a maximum of 10.5 nm thick

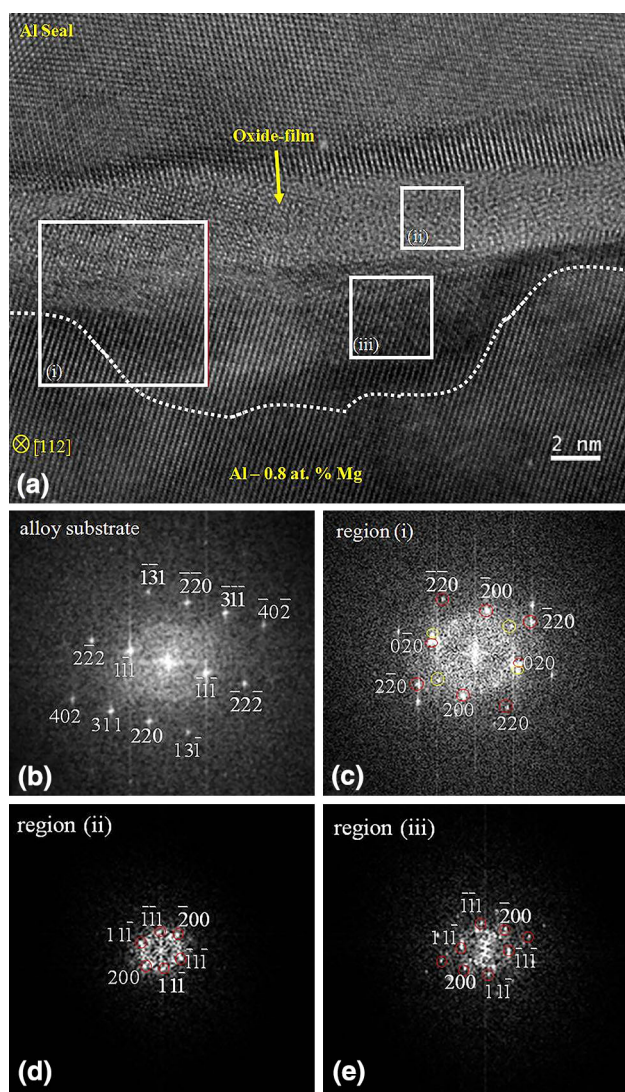


**Fig. 3** (Color Online) **a** HR-TEM micrograph of the oxide film formed by oxidizing the native  $\sim 2.5$  nm thick amorphous  $\text{Al}_2\text{O}_3$ -coated Al-0.8 at.% Mg alloy substrate for  $t = 2$  h at  $T = 600$  K and  $p\text{O}_2 = 1 \times 10^{-2}$  Pa. The direction of the primary electron beam was along the zone axis  $[\bar{1}12]$  of the investigated grain of the polycrystalline alloy substrate. **b**, **c**, **d** and **e** Fourier transformations of the areas comprising only substrate, (i) (comprising both substrate and oxide), (ii) (comprising only oxide), and (iii) (comprising both substrate and diffused oxide into the substrate) as indicated in **a**, respectively. The dotted marked regions within the substrate demonstrate the oxide diffused region into the alloy substrate as identified from the Fourier transformation of these regions

oxide-film. Presence of these (diffused) oxides at the Al-Mg sub surface (henceforth known as oxide pockets) may be due to higher  $T$  induced inward diffusion of oxygen anions through the oxide-film grain boundaries leading to oxidation reactions at the alloy/oxide interface. It should be noted that, thickening (i.e., further growth) of the already existing native  $am\text{-Al}_2\text{O}_3$  on the Al-Mg alloy substrate due to oxidation at  $T = 600$  K for  $t = 2$  h and at  $p\text{O}_2$  of

$1 \times 10^{-2}$  Pa (as is the case here) can only happen due to the addition of the newly formed (Al, Mg)-oxides (due to oxidation reaction) on to it, facilitated by either outward diffusion of  $\text{Al}^{3+}$  and/or  $\text{Mg}^{2+}$  cationic species to the oxide-film surface and/or inward diffusion of  $\text{O}^{2-}$  anionic species to the alloy/oxide interface through the existing oxide-film. As observed in literature [17], at lower temperature of  $T < 500$  K, further film growth by outward diffusion of cationic species through vacancies and interstitials happens in a much faster rate than that of the anion diffusion through the oxide grain boundaries. This is because, predominantly amorphous oxides are formed at lower temperatures. Only at higher temperature of  $T > 500$  K, due to the formation of the (partially) crystalline oxides, inward anion transport as well as the outward cation transport become significant. Moreover, formation of oxide pockets at the Al-Mg alloy sub-surface signifies the inward diffusion of oxygen anions (through the oxide grain boundaries) to the alloy/oxide interface followed by oxidation reactions at these interfaces. It should be noted that, further oxide-film growth (due to oxidation of the native oxide-coated Al-Mg alloy substrate) by outward diffusion of cations has not been completely excluded here.

Overall, this oxide-film is found to consist of a mixed amorphous, (poly) crystalline and an intermediate amorphous-to-crystalline transition regions, with the crystalline regions consisting of mostly MgO. Presence of the mixed oxide at this elevated  $T$  (unlike the formation of entirely crystalline oxides on pure metal substrates at these  $T$ ) [12, 13, 17] may be attributed to the initially present native  $am\text{-Al}_2\text{O}_3$  before the onset of oxidation. It should be noted that, the absence of a uniformly thick (thickness of  $2.49 \pm 0.18$  nm) amorphous and/or crystalline  $\text{Al}_2\text{O}_3$  layer at the oxide-film surface or at the alloy/oxide interface or within the irregularly grown oxide-film in this study rules out the possibility of entirely crystallizing this initially present  $am\text{-Al}_2\text{O}_3$  and/or being trapped inside the newly formed (Al, Mg)-oxide. Moreover, presence of (predominantly) MgO in the crystalline regions of this grown oxide-film further adds against complete crystallization of this natively grown  $am\text{-Al}_2\text{O}_3$ . As HR-TEM cannot map elemental distribution in the amorphous and amorphous-to-crystalline transition regions of this oxide-film, identifying the presence of Mg-oxide and Al-oxide in these oxide regions can not be made. However, the overall Al-to-Mg-ratio in the entire oxide film is found to be  $0.49 \pm 0.06$  by AR-XPS indicating presence of large quantities of Mg-oxide as compared to Al-oxide in this film.

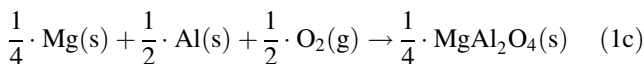
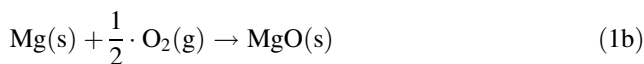
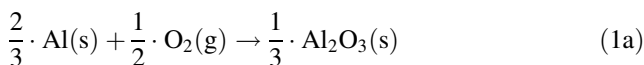
As evidenced from the measurement of the angles and lengths between the spots that arises from the Fourier transformation of the HR-TEM images (see circled spots of Fig. 3e), the diffused oxide regions (into the Al-Mg alloy

sub-surface) are found to be crystalline in nature, consisting of  $\gamma\text{-Al}_2\text{O}_3$  (with lattice parameter of 4.03 Å and crystallographic orientation relationship (COR) with that of the substrate as  $(\bar{1}12)_{\text{Al-Mg}} \parallel (011)_{\text{Al}_2\text{O}_3}; [\bar{1}12]_{\text{Al-Mg}} \parallel [011]_{\text{Al}_2\text{O}_3}$ ). Further, the grown *cr*-MgO are found to have COR with that of the substrate as:  $(\bar{1}12)_{\text{Al-Mg}} \parallel (2\bar{3}3)_{\text{MgO}}; [\bar{1}12]_{\text{Al-Mg}} \parallel [2\bar{3}3]_{\text{MgO}}$  (calculated lattice parameters of 4.41 and 4.46 Å from oxide-film of region (iii) in Fig. 1 and region (ii) in Fig. 2 respectively) and  $(\bar{1}12)_{\text{Al-Mg}} \parallel (001)_{\text{MgO}}; [\bar{1}12]_{\text{Al-Mg}} \parallel [(001)_{\text{MgO}}$  (calculated lattice parameter of 4.50 Å; see oxide-film of region (i) of Fig. 3). Similarly,  $\gamma\text{-Al}_2\text{O}_3$  is found to have COR with that of the substrate as:  $(\bar{1}12)_{\text{Al-Mg}} \parallel (\bar{1}22)_{\text{MgO}}; [\bar{1}12]_{\text{Al-Mg}} \parallel [\bar{1}22]_{\text{MgO}}$  (calculated lattice parameter of 3.66 Å; see oxide-film of region (i) in Fig. 2). These observed high indexed COR with that of the substrate may be attributed to kinetics rather than thermodynamics and may also be associated to the growth of oxide-film on a native *am*- $\text{Al}_2\text{O}_3$  coated (instead of a cleaned) Al–Mg alloy substrate. It has already been demonstrated that, at initial stages of oxidation, when oxide-film thickness is low, amorphous oxides (consisting of *am*- $\text{Al}_2\text{O}_3$ ) grow on Al–Mg alloy substrate rather than the crystalline one (consisting of *cr*-MgO) because of the dominant contribution of the interface and surface energies over the bulk Gibbs free energies (see Sect. 4). However, with increasing oxide-film thickness, the thickness dependent bulk free energy terms become dominant over the interface energy terms in the total Gibbs free energy expressions, thus, forming crystalline oxides at higher oxide-film thicknesses. Finally, amorphous to crystalline transition regions are observed in between the amorphous and crystalline oxide regions (see region (ii) in Fig. 1). Incidentally, some reflections of *cr*-MgO (i.e., region (iii), see Fig. 1d) are also observed in this amorphous-to-crystalline transition region (i.e., region (ii), see Fig. 1c) with a rotation of  $\sim 11^\circ$  indicating the formative state of the similarly oriented *cr*-MgO type of oxide-film in region (ii) as that of region (iii). This may be attributed to the process of strain relaxation between the (predominantly) amorphous and (completely) crystalline regions in the oxide-film. Additional unidentified reflections are observed in the Fourier transformed HR-TEM images of the oxide-films, indicating presence of partially ordered oxides of either  $\gamma\text{-Al}_2\text{O}_3$  or *cr*-MgO (regions (i) and (ii) of Fig. 2).

Ordering of the amorphous region is observed at the interface between the amorphous oxide-film and the Al capping layer (see Fig. 1a; lines are drawn showing start of crystallization process in these amorphous regions of the oxide-film adjacent to the crystalline Al capping layer). This is consistent with the reported HR-TEM observations, confirming the initiation of the ordering phenomena from the interface of an original amorphous oxide [35].

#### 4 Thermodynamics of the Growth of Both the Amorphous and Crystalline Oxides on <AlMg> Alloy Substrate

To understand thermodynamically the growth of a particular oxide on <AlMg> alloy substrate with respect to various experimental parameters, such as, Mg alloying elemental content at the alloy/oxide interface ( $x_{\text{Mg}}^i$ ), growth temperature ( $T$ ) and oxide-film thicknesses ( $h_{(\text{oxide})}$ ), total Gibbs energies ( $G_{(\text{oxide})}^{\text{cell}}$ ) of all possible six amorphous and crystalline oxide phases (i.e.,  $\{\text{Al}_2\text{O}_3\}$ ,  $\{\text{MgO}\}$ ,  $\{\text{MgAl}_2\text{O}_4\}$ ,  $\langle\text{Al}_2\text{O}_3\rangle$ ,  $\langle\text{MgO}\rangle$  and  $\langle\text{MgAl}_2\text{O}_4\rangle$ , per unit area of  $\{\text{MgO}\}$  unit cell; chosen arbitrarily) on the most densely packed surface of <AlMg> alloy substrate were compared theoretically as a function of  $x_{\text{Mg}}^i$ ,  $T$  and  $h_{(\text{oxide})}$  varying in the ranges of 0–0.5, 298.15–900 K and up to 5 nm respectively [15, 34]. In this calculation, relevant oxide “unit cells” containing same molar quantities of oxygen and thus different molar quantities of oxide phases (due to their different metal-to-oxygen atomic ratios) are considered. These corresponding oxidation reactions using per mole of O reactants are described as:



Along with the bulk Gibbs free energies of these oxides, this model also considers alloy/oxide interface energies and oxide surface energies towards calculating the total Gibbs energies. It is found that, at lower oxide-film thicknesses, all these considered amorphous oxide phases have lower total Gibbs energies than their crystalline counterparts because of their lower (positive) surface energy and (maximum negative) interface energy contributions over the less negative bulk Gibbs free energy contribution terms of the total energy expressions [10, 15, 34], whereas, at higher  $h_{(\text{oxide})}$ , the thickness dependent bulk Gibbs free energy contributions become dominant over the surface- and interface energy contribution terms, thereby dominating the growth of crystalline oxides at increased  $h_{(\text{oxide})}$ . Moreover, it is observed that,  $G_{\{\text{Al}_2\text{O}_3\}}^{\text{cell}}$  is lowest (i.e., most negative) at lower oxide-film thicknesses irrespective of  $T$  and  $x_{\text{Mg}}^i$ , beyond which  $G_{\langle\text{MgO}\rangle}^{\text{cell}}$  becomes lowest for all  $T$  and  $x_{\text{Mg}}^i$ , indicating that, at lower oxide-film thicknesses, amorphous  $\{\text{Al}_2\text{O}_3\}$  forms thermodynamically, whereas, crystalline  $\langle\text{MgO}\rangle$  overgrowth becomes thermodynamically favored at higher oxide-film thicknesses. The critical oxide-film thickness,  $h_{\langle\text{MgO}\rangle}^{\text{critical}}$  (at which  $G_{\{\text{Al}_2\text{O}_3\}}^{\text{cell}} = G_{\langle\text{MgO}\rangle}^{\text{cell}}$ ), beyond

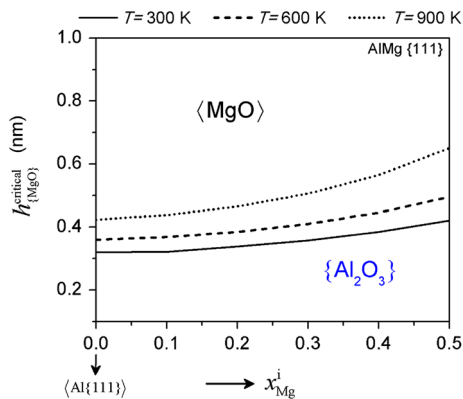


**Fig. 4** Critical oxide-film thickness,  $h_{[MgO]}^{critical}$ , beyond which the crystalline  $\langle MgO \rangle$  overgrowth on the most densely packed surface of the  $\langle AlMg \rangle$  substrate becomes thermodynamically more stable than the amorphous  $\{ Al_2O_3 \}$  overgrowth on the same alloy substrate, as a function of the Mg alloying content at the alloy/oxide interface ( $x_{Mg}^i$ ) at growth temperatures of  $T = 300, 600$  and  $900$  K. For details, see Sect. 4

which  $\langle MgO \rangle$  overgrowth on the most densely packed  $\langle AlMg \rangle$  alloy substrate is more stable thermodynamically than the  $\{ Al_2O_3 \}$  overgrowth, which varies from 0.32 to 0.42 nm at  $T = 300$  K and 0.42 to 0.65 nm at  $T = 900$  K for  $x_{Mg}^i$  varying between 0 and 0.5 respectively (see Fig. 4). The various low-index crystallographic surfaces of  $\langle AlMg \rangle$  alloy substrate are found to have no additional effect towards the growth of thermodynamically preferred oxide phases on these alloy substrates. These thermodynamic predictions can be validated with the experimental observation in the present study, where, amorphous  $Al_2O_3$  is found to form at room temperature and under atmospheric pressure on an Al–Mg alloy substrate by aging for a week. Similarly, (predominantly) crystalline MgO is found to form on this alloy substrate after subjected to higher temperature oxidation for a longer time, which results into the growth of a relatively thicker oxide-film.

## 5 Conclusions

HR-TEM investigations on the oxide-film grown on an amorphous native  $Al_2O_3$ -coated Al-0.8 at.% Mg alloy substrate at  $T = 600$  K for  $t = 2$  h and at  $pO_2$  of  $1 \times 10^{-2}$  Pa revealed the oxide-film to be non-uniformly thick with thicknesses varying in the range of 1.50–4.60 nm, although the thickness of the diffused oxide region into the Al–Mg alloy substrate formed a maximum of 10.5 nm thickness. Overall, this non-uniformly thick oxide-film was found to consist of a mixed amorphous, (poly) crystalline and an amorphous-to-crystalline transition regions, whereas, the diffused oxide regions into the Al–Mg alloy substrate was found to consist of only crystalline oxide. As evidenced

from the local lattice parameters estimated using HR-TEM in this study, the crystalline regions of the irregularly thick oxide-film was found to consist of mostly thermodynamically favored MgO, whereas, the diffused oxide regions into the Al–Mg alloy substrate was found to consist of only  $\gamma-Al_2O_3$ . The local lattice parameter values as calculated from the Fourier transformed crystalline regions were found to vary between 3.60 and 3.98 Å for  $\gamma-Al_2O_3$  and 4.41–4.50 Å for MgO with higher lattice mismatch crystallographic orientation relationships with that of the substrate. These observed anomalies in the local lattice parameter values were attributed to the presence of local strain in the oxide-film resulting from the mixed amorphous, crystalline and amorphous-to-crystalline transition regions as well as due to the formation of multiple phases (i.e., Al-oxide, Mg-oxide) in the oxide-film.

**Acknowledgments** The experiments were carried out in Max Planck Institute for Intelligent Systems (formerly known as Max Planck Institute for Metals Research), Stuttgart, Germany. The authors are indebted to Prof. Eric J. Mittemeijer for the provision of oxidation and in situ AR-XPS and MBE facilities, Dr. Lars P.H. Jeurgens for his invaluable discussions, Dr. P.A. van Aken for the provision of TEM facilities, Dr. Gunther Richter for taking the HR-TEM images and to Mrs. U. Eigenthaler for the FIB preparation of the TEM lamellae.

## References

- Nolte P, Stierle A, Jin-Phillipp N Y, Kasper N, Schulli T U, and Dosch H, *Science* **321** (2008) 1654.
- Lyapin A, Jeurgens L P H, Graat P C J, and Mittemeijer E J, *J Appl Phys* **96** (2004) 7126.
- Jeurgens L P H, Vinodh M S, and Mittemeijer E J, *Acta Mater.* **56** (2008) 4621.
- Pasquarello A, and Stoneham A M, *J Phys Condensed Matter* **17** (2005) V1.
- Freund H J, *Surf Sci* **601** (2007) 1438.
- Koyama M, Kamimuta Y, Koike M, Suzuki M, and Nishiyama A, *Jpn J Appl Phys* **43** (2004) 1788.
- Dai Z R, Pan Z W, and Wang Z L, *Adv Funct Mater* **13** (2003) 9.
- Comini E, Faglia G, Sberveglieri G, Pan Z, and Wang Z L, *Appl Phys Lett* **81** (2002) 1869.
- Gupta A, Li X W, and Xiao G, *Appl Phys Lett* **78** (2001) 1894.
- Jeurgens L P H, Wang Z M, and Mittemeijer E J, *Int J Mater Res* **100** (2009) 1281.
- Reichel F, Jeurgens L P H, and Mittemeijer E J, *Acta Mater* **56** (2008) 2897.
- Reichel F, Jeurgens L P H, Richter G, and Mittemeijer E J, *J Appl Phys* **103** (2008) 093515.
- Reichel F, Jeurgens L P H, Richter G, van Aken P A, and Mittemeijer E J, *Acta Mater* **55** (2007) 6027.
- Panda E, Jeurgens L P H, and Mittemeijer E J, *Surf Sci* **604** (2010) 588.
- Panda E, Jeurgens L P H, and Mittemeijer E J, *Acta Mater* **58** (2010) 1770.
- Snijders P C, Jeurgens L P H, and Sloof W G, *Surf Sci* **589** (2005) 98.
- Jeurgens L P H, Sloof W G, Tichelaar F D, and Mittemeijer E J, *Thin Solid Films* **418** (2002) 89.
- Lea C, and Molinari C, *J Mater Sci* **19** (1984) 2336.

19. Lea C, and Ball J, *Appl Surf Sci* **17** (1984) 344.
20. Brock A J, and Heine M A, *J Electrochem Soc* **119** (1972) 1124.
21. Hart R K, and Maurin J K, *Surf Sci* **20** (1970) 285.
22. Goldstein B, and Dresner J, *Surf Sci* **71** (1978) 15.
23. Ritchie I M, Sanders J V, and Weickhardt P L, *Oxid Met* **1** (1971) 91.
24. Doherty P E, and Davis R S, *J Appl Phys* **34** (1963) 619.
25. Thomas K, and Roberts M W, *J Appl Phys* **32** (1961) 70.
26. Bahadur A, *J Mater Sci* **22** (1987) 1941.
27. van Beek H J, and Mittemeijer E J, *Thin Solid Films* **122** (1984) 131.
28. Brock A J, and Pryor M J, *Corros Sci* **13** (1973) 199.
29. Pryor M J, *Oxid Met* **3** (1971) 271.
30. Smeltzer W, *J Electrochem Soc* **105** (1958) 67.
31. Marton D, Josepovits V K, and Csandy A, *Surf Interface Anal* **1** (1979) 132.
32. Scamans G, and Butler E P, *Metall Trans A* **6A** (1975) 2055.
33. Panda E, Jeurgens L P H, and Mittemeijer E J, *J Appl Phys* **106** (2009) 114913.
34. Ajmera D, and Panda E, *Corros Sci* **102** (2016) 425.
35. Oh S H, Kauffmann Y, Scheu C, Kaplan W D, and Rühle M, *Science* **310** (2005) 661.